Superelastic oxide micropillars enabled by surface tension–modulated 90° domain switching with excellent fatigue resistance

Yingwei Li[a,b,c,d,1,2], Kangjie Chu[e,f,1], Chang Liu[g,h,1], Peng Jiang[i,1], Ke Qu[i,j], Peng Gao[j,k], Jie Wang[g,h,2], Fuzeng Ren[e,2], Qingping Sun[f], Longqing Chen[l,m,n], and Jiangyu Li[d,e,i,2]

[a]School of Civil Engineering, Wuhan University, 430072 Wuhan, Hubei, China; [b]State Key Laboratory of Water Resources and Hydropower Engineering Science, Wuhan University, 430072 Wuhan, Hubei, China; [c]Hubei Key Laboratory of Theory and Application of Advanced Materials Mechanics, Wuhan University of Technology, 430070 Wuhan, Hubei, China; [d]Guangdong Provincial Key Laboratory of Functional Oxide Materials and Devices, Southern University of Science and Technology, 518055 Shenzhen, Guangdong, China; [e]Department of Materials Science and Engineering, Southern University of Science and Technology, 518055 Shenzhen, Guangdong, China; [f]Department of Mechanical and Aerospace Engineering, The Hong Kong University of Science and Technology, Clear Water Bay, Hong Kong, China; [g]Department of Engineering Mechanics, Zhejiang University, 310027 Hangzhou, Zhejiang, China; [h]Key Laboratory of Soft Machines and Smart Devices of Zhejiang Province, Zhejiang University, 310027 Hangzhou, Zhejiang, China; [i]Shenzhen Key Laboratory of Nanobiomechanics, Shenzhen Institutes of Advanced Technology, Chinese Academy of Sciences, 518055 Shenzhen, Guangdong, China; [j]Electron Microscopy Laboratory, School of Physics, Peking University, 100871 Beijing, China; [k]Interdisciplinary Institute of Light-Element Quantum Materials and Research Center for Light-Element Advanced Materials, Peking University, 100871 Beijing, China; [l]Department of Materials Science and Engineering, The Pennsylvania State University, University Park, PA 16802; [m]Department of Engineering Science and Mechanics, The Pennsylvania State University, University Park, PA 16802; and [n]Department of Mathematics, The Pennsylvania State University, University Park, PA 16802

Edited by David A. Weitz, Harvard University, Cambridge, MA, and approved April 25, 2021 (received for review December 8, 2020)

Superelastic materials capable of recovering large nonlinear strains are ideal for a variety of applications in morphing structures, reconfigurable systems, and robots. However, making oxide materials superelastic has been a long-standing challenge due to their intrinsic brittleness. Here, we fabricate ferroelectric $BaTiO_3$ (BTO) micropillars that not only are superelastic but also possess excellent fatigue resistance, lasting over 1 million cycles without accumulating residual strains or noticeable variation in stress–strain curves. Phase field simulations reveal that the large recoverable strains of BTO micropillars arise from surface tension–modulated 90° domain switching and thus are size dependent, while the small energy barrier and ultralow energy dissipation are responsible for their unprecedented cyclic stability among superelastic materials. This work demonstrates a general strategy to realize superelastic and fatigue-resistant domain switching in ferroelectric oxides for many potential applications.

superelasticity | oxide micropillars | surface tension | ferroelectric switching | fatigue

Superelastic materials are capable of recovering large amount of nonlinear "plastic" strains, way beyond their linear elastic regimes (1–4). They are ideal for a variety of applications from morphing structures, reconfigurable systems, to robots (5–8). The effects have traditionally been associated with macroscopically compliant/ductile rubbers (2) or microscopically phase-transforming shape memory alloys (SMAs) (7–11). The only macroscopically brittle oxide recently discovered to be superelastic is ZrO_2-based micropillars or particles (12–20), which is realized via austenite-martensite phase transformation similar to SMAs. Although ultimate strengths approaching the theoretical limit have been demonstrated in nanoscale samples (21, 22), long fatigue life is elusive, which is arguably more important for most applications. As a matter of fact, poor fatigue life has been a long-standing challenge for oxide ceramics in general (23, 24). Even for ductile SMAs that enjoy excellent fatigue life, irrecoverable residual strains gradually accumulate over cycling, leading to substantial variations in stress–strain curves at different cycles (9, 10, 25). We overcome these difficulties by reporting superelastic barium titanate ($BaTiO_3$ [BTO]) micropillars enabled by surface tension–modulated 90° domain switching, which exhibit excellent fatigue resistance, while bulk BTO crystals or ceramics are rather brittle. The demonstration of over one million cycles of loading and unloading without accumulating residual strains or noticeable variation in stress–strain curves is unprecedented among superelastic materials.

BTO is a ferroelectric oxide exhibiting modest piezoelectric strains around 0.1 to 0.2% (26) and fracture toughness of ∼1 $MPa \cdot m^{1/2}$, and thus it is quite brittle (27). Considerable research efforts have been devoted to enhancing its electric field–induced strain via 90° ferroelectric domain switching (28–30). However, the process is often irreversible, and external mechanisms such as restoring force (28, 29) and internal mechanisms such as defect pinning (30) have to be invoked to make the electrostrain recoverable. Nevertheless, it hints at the possibility of BTO being made superelastic by taking advantage of the stress-induced 90° domain switching (6). Earlier works suggest that surface tension induces an in-plane compressive stress that favors the axial polarization in one-dimensional ferroelectrics at small size (31, 32), which may provide the necessary restoring mechanism for the stress-switched domains. Thus, if a compressive axial force is applied, reversible domain switching may occur during unloading, leading to superelasticity. To verify this hypothesis, we fabricated

Significance

We demonstrate the micropillars of normally brittle $BaTiO_3$ (BTO) are superelastic as well as fatigue resistant over 1 million cycles without accumulating residual strains or noticeable variation in stress–strain curves over cycles. The mechanism of reversible 90° domain switching identified in our work is advantageous over the conventional phase transition mechanism as found in ZrO_2 and shape memory alloys, and it is not limited to BTO. Therefore, our work offers a promising strategy for realizing fatigue-resistant superelasticity in otherwise brittle ferroelectric materials.

Author contributions: Y.L. and J.L. designed research; Y.L., K.C., C.L., P.J., K.Q., J.W., and F.R. performed research; Q.S. contributed new reagents/analytic tools; Y.L., K.C., C.L., P.G., J.W., F.R., Q.S., L.C., and J.L. analyzed data; and Y.L., J.W., F.R., L.C., and J.L. wrote the paper.

The authors declare no competing interest.

This article is a PNAS Direct Submission.

[1]Y.L., K.C., C.L., and P.J. contributed equally to this work.

[2]To whom correspondence may be addressed. Email: yingweili@whu.edu.cn, jw@zju.edu.cn, renfz@sustech.edu.cn, or lijy@sustech.edu.cn.

This article contains supporting information online at https://www.pnas.org/lookup/suppl/doi:10.1073/pnas.2025255118/-/DCSupplemental.

Published June 11, 2021.

single-crystalline BTO micropillars from [001]-oriented bulk crystals (*SI Appendix*, Fig. S1*A*) via focused ion beam (FIB), as detailed in *Materials and Methods* and *SI Appendix*, Fig. S1*B*. The diameters (Φ) of the micropillars range from 0.5 μm to 5 μm, with their height to diameter ratio fixed at 3. No visible defects can be seen from the scanning electron microscopy (SEM) images of these micropillars shown in Fig. 1 *A*–*D*, and their surfaces appear to be quite smooth, suggesting that no apparent damages are induced by FIB.

BTO Micropillars Fabrication and Stress–Strain Curve Measurement

We first characterize BTO single crystals used for micropillars. The dielectric measurement of the BTO single crystals shows an anomaly at 135 °C (*SI Appendix*, Fig. S2*A*), corresponding to its cubic-tetragonal phase transition. The X-ray diffraction (XRD) of the unpoled BTO single crystal confirms its tetragonal symmetry with a c/a ratio of 1.01 at 25 °C (*SI Appendix*, Fig. S2*B*). The crystal was then poled along the [001] axis as schematically shown in *SI Appendix*, Fig. S1*A*. Under a cyclic electric field loading, the crystal exhibits typical ferroelectric hysteresis and butterfly loops (*SI Appendix*, Fig. S3*A*) with a spontaneous polarization of 26 $\mu C/cm^2$ and an electrostrain of 0.012%. The strain is substantially smaller than that expected from c/a ratio due to the lack of 90° domain switching (28–30). A compressive stress of 15 MPa, on the other hand, is sufficient to completely depolarize the crystal via 90° domain switching, resulting in residual strains as large as 0.95% (*SI Appendix*, Fig. S3*B*), close to its spontaneous strains of 1.05%.

We then examine the mechanical responses of BTO micropillars by compressing them along their long axis using a Hysitron TI-950 nanoindentor with a diamond flat punch. All the experiments are conducted at room temperature that is far from the phase transition temperature of BTO. Considering the fact that stress usually increases the transition temperature of BTO (33), the stress-induced phase transformation is not expected to occur in BTO micropillars. Measuring the load-displacement of the micropillars accurately is quite challenging due to the inevitable deformation of the substrate. Therefore, we also employed the dual-pillar method recently developed in ref. 34 to study such effects (*SI Appendix*, Fig. S4). Indeed, we found about 10~20% overestimation of strains. All of the analyses are based on the corrected stress–strain curves, while uncorrected ones are presented in *SI Appendix*, Fig. S5. For micropillars with relatively large diameters (e.g., 5 μm) (Fig. 1*E*), the first cycle stress–strain curve consists of an initial linear regime, a plateau regime corresponding to rapid 90° domain switching during which the strain accumulates without increasing stress, and then a subsequent linear regime followed by the unloading curve with a slope similar to the second linear regime during loading. This results in a large residual strain of 0.7%, very similar to the stress–strain curve of *SI Appendix*, Fig. S3*B* for the bulk crystal. The second cycle of loading and unloading is drastically different from the first one, exhibiting linear elastic behavior since 90° domain switching is already exhausted in the first cycle.

However, when the micropillar diameter decreases to 2 μm (Fig. 1*F*), the transition between initial linear regime and stress plateau in the stress–strain curve become less well defined, and the unloading after the subsequent linear regime (up to 0.98% of

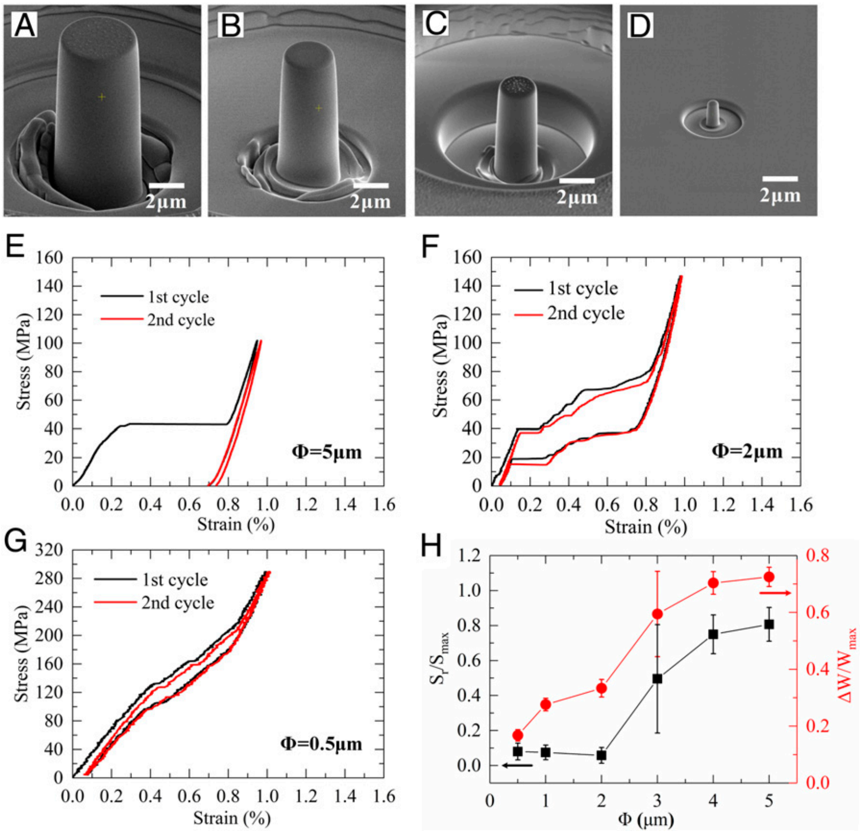

Fig. 1. Superelastic BTO micropillars below a critical size. (*A*–*D*) SEM images of the micropillars with Φ = 5, 3, 2, and 0.5 μm. (*E*–*G*) The first and second cycles of stress–strain curves for BTO micropillars with Φ = 5, 2, and 0.5 μm. (*H*) S_r/S_{max} and $\Delta W/W_{max}$ during the first cycle for BTO micropillars of different diameters. Here, S_r and S_{max} denote the residual strain and the maximum strain (*SI Appendix*, Fig. S6*A*), while ΔW and W_{max} are energy dissipated and stored in the first cycle, respectively (*SI Appendix*, Fig. S6*F*).

strain) no longer follows the linear slope. Instead, the unloading curve goes through a plateau (via reversed 90° domain switching) followed by another linear regime, resulting in almost complete recovery of the strain with a residual strain as small as 0.05%. The second cycle loading and unloading curve closely follows the first cycle, with almost an identical residual strain of 0.05% referenced to the virgin state. Therefore, we achieve superelastic behavior in the micropillar with a diameter of 2 μm, although there is still large hysteresis. When the diameter is further reduced to 0.5 μm (Fig. 1*G*), we can hardly differentiate the linear, plateau, and subsequent linear regimes in the loading curve, and only slight change in slopes can be seen throughout the loading range. After unloading, the large strain of 1.0% is almost completely recovered with a residual strain of 0.06%, while the hysteresis is much smaller than the 2-μm diameter micropillar. The second cycle closely follows the first one as well, and the behavior is drastically different from that of the bulk crystal shown in *SI Appendix*, Fig. S3*B*. Stress–strain curves for micropillars of other diameters are presented in *SI Appendix*, Fig. S6.

It is also interesting to examine the ratios of residual strain (S_r/S_{max}) as well as energy dissipated ($\Delta W/W_{max}$) for micropillars of different diameters in the first cycle, as summarized in Fig. 1*H*, for which five specimens are tested for each diameter. The size effect is evident, showing a clear transition from 3 to 2 μm with sharp decreases in both residual strain and hysteresis. Note that some micropillars with $\Phi = 3$ μm can recover a large strain in the first few cycles and then lose its recoverability upon further cycling (*SI Appendix*, Fig. S6 *D* and *E*), resulting in uncharacteristically large data scattering seen in Fig. 1*H*.

To understand the large recoverable strain in the BTO micropillars at small size, we carry out the piezoresponse force microscopy (PFM) mapping (*SI Appendix*, Fig. S7) and switching (*SI Appendix*, Fig. S8) experiments, which confirm that the micropillars are ferroelectric with switchable polarization. The 90° domain switching process under stress has also been captured by in situ transmission electron microscopy (TEM; *SI Appendix*, Fig. S9 and Movie S1), acquired from a thin plate sample instead. However, this switching mechanism alone is not sufficient to explain the remarkable superelastic recovery of large strain in micropillars with smaller diameters. One of the possible mechanisms for the strain recovery is the effect of depolarization field. However, the micropillars have the same aspect ratio while the depolarization field is independent of the size, and thus it cannot explain the difference in the strain recovery for micropillars of different diameters. It has also been suggested that surface tension may play an important role in micropillars due to their small sizes, and the magnitude of surface tension increases with decreasing micropillar diameter (31, 32, 35). In order to verify this effect, we carried out phase field simulation as detailed in *Materials and Methods*, taking into account the surface tension that is inversely proportional to the radius of the micropillars (31, 32).

Thermodynamic Analysis and Phase Field Simulation

We first examine the thermodynamic stability of different polarization states under the influence of surface tension. For easier visualization, we only considered the competition between P_1 and P_3. In the absence of surface tension, there are four degenerate wells in the thermodynamic potential energy surface as a function of polarization component P_1 and P_3 (Fig. 2*A*), corresponding to equivalent $a^{+/-}$ and $c^{+/-}$ domains in a bulk crystal. Under the influence of surface tension, compressive radial stresses of $\sigma_{11} = \sigma_{22} = 2\gamma/\Phi$ appear on the side surface of the micropillar (31, 32). The energetics of the 5-μm micropillar is only slightly modified with four wells remaining (Fig. 2*B*), and $c^{+/-}$ domains become slightly favored over $a^{+/-}$ domains as expected. A micropillar with $\Phi = 0.5$ μm, on the other hand, is drastically different, wherein $a^{+/-}$ domains become unstable as the corresponding energy wells disappear, leaving only 2 wells representing the $c^{+/-}$ domains (Fig. 2*C*). This can be seen more clearly in the energy curve in Fig. 2*D* following the path from $a^{+/-}$ domains to c^{+} domain as identified by the black curve in Fig. 2*C*, wherein one energy well at c^{+} domain is evident while $a^{+/-}$ domains are energetically unstable. This suggests that smaller micropillars contain larger fractions of more stable c domains, which is consistent with PFM poling experiment (*SI Appendix*, Fig. S8). The energetics, however, can be shifted by a compressive axial stress, which stabilizes $a^{+/-}$ domains resulting in reappearance of two corresponding energy wells (Fig. 2*D*). At a high compressive stress of 200 MPa, the energetic balance is tipped, and the $a^{+/-}$ domains become more stable, while further increase in compressive stress can destabilize c^{+} domain. As such, stress-induced 90° domain switching occurs, leading to a large strain that can be recovered upon unloading due to surface tension.

The superelastic stress–strain curve of the 0.5-μm micropillar obtained from three-dimensional phase field simulations shown in Fig. 2*E* agrees well with the corresponding experiment observation. The domain evolution during superelastic loading and unloading is shown in Fig. 2 *G*–*K* (corresponding to points marked on the stress–strain curve in Fig. 2*E*) and Movie S2. Note that the end surfaces have predominantly in-plane polarization in the virgin state while the majority of interior polar vectors are axial, presumably to reduce the depolarization energy, and this is consistent with the large lateral PFM signal seen in *SI Appendix*, Fig. S7. For the 5-μm micropillar, on the other hand, the strain from 90° domain switching is not recoverable after unloading (*SI Appendix*, Fig. S10*B*), resulting in a stress–strain curve shown in Fig. 2*F* and *SI Appendix*, Fig. S10*C* with a large residual strain. The lack of switching recovery for the 5-μm micropillar is shown in *SI Appendix*, Fig. S10 *D*–*H* and Movie S3. Therefore, the size effect observed from the experimental stress–strain curves of BTO micropillars is explained very well by the phase field simulation, particularly the switching and recovery of 90° domains during loading and unloading. It can also be captured by the variation of surface stress versus diameter Φ presented in *SI Appendix*, Fig. S11, from which the critical diameter can be identified. In fact, significant size effect has been reported for micropillars, wires, particles, and membranes of various materials including metals (36–38), ceramics (12–20, 39), SMAs (8–10, 40), and ferroelectrics (6, 31, 32, 35, 41), and some of the observations have been attributed to surface tension (6, 31, 32, 35, 36, 41). For example, Diao et al. found that, in gold nanowires, irreversible phase transition occurs when its cross-sectional size approaches a few nanometers due to much increased surface-to-volume ratio (36), while Dong et al. reported that the surface stress can significantly modulates the energy landscape of BTO membranes, allowing the dipoles to rotate continuously during bending (6).

Fatigue and Strength Characterization

One of the major issues facing oxide micropillars is their poor fatigue life. Our BTO micropillars, on the other hand, demonstrate remarkable fatigue resistance as seen in Fig. 3*A*. Indeed, after loading and unloading for one million cycles, the stress–strain curves of a micropillar with $\Phi = 0.58$ μm show no sign of degradation, recovering strains as large as 1.0% under a stress of 203 MPa and with a residual strain as small as 0.08% (The original data are presented in *SI Appendix*, Fig. S12.) Furthermore, there is negligible variation in the stress–strain curves from the second cycle and on. Micropillars with diameters ≤2 μm show similar fatigue characteristics, going up to 10 thousand cycles without failure (*SI Appendix*, Fig. S13). The SEM images of the as-milled 0.58-μm micropillar (Fig. 3*B*) and after one million cycles (Fig. 3*C*) show virtually no difference, with no damages or defects induced by cycling seen, demonstrating its excellent fatigue resistance.

We also measure the ultimate compressive strength of BTO micropillars with $\Phi = 0.5$ μm, reaching an ultrahigh strength of 5.3 GPa, which is two orders of magnitude higher than bulk BTO of only 30 MPa (42). It actually approaches the theoretical strength of BTO crystal estimated to be 7 GPa based on the

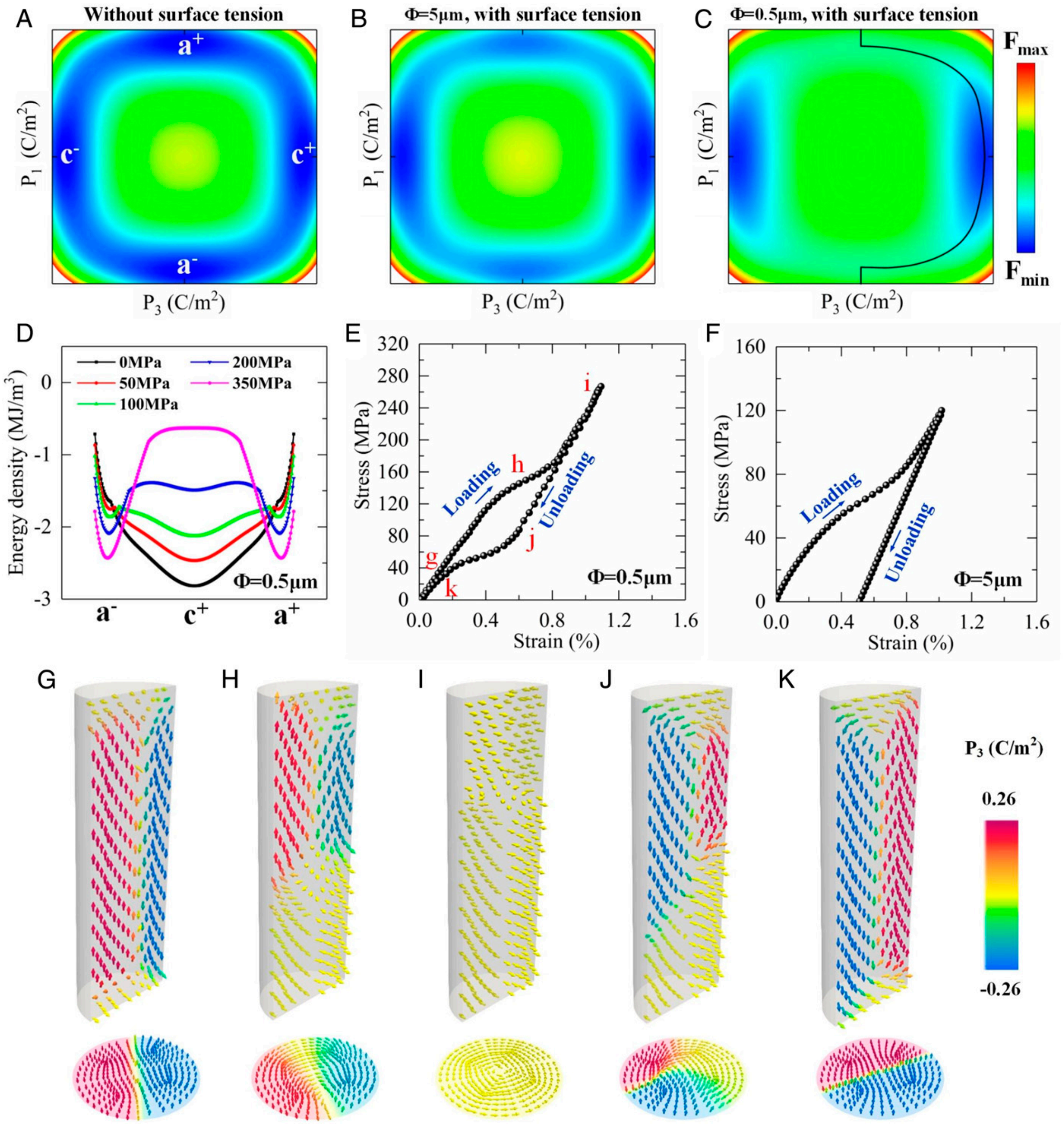

Fig. 2. Superelasticity via surface tension–modulated ferroelectric switching. Free energy contours calculated based on the Landau–Devonshire theory for BTO micropillars without surface tension, regardless of diameter (*A*), and with surface tension, having $\Phi = 5$ μm (*B*) and 0.5 μm (*C*); $c^{+/-}$ and $a^{+/-}$ represent the corresponding domains. (*D*) Free energy profiles along the path marked by the black curve in *C* for BTO micropillar with $\Phi = 0.5$ μm under different compressive stresses. Stress–strain curves calculated by phase field simulation for BTO micropillar with $\Phi = 0.5$ μm (*E*) and 5 μm (*F*). (*G*–*K*) Representative domain configurations in 0.5-μm micropillar during loading and unloading, corresponding to the points of *G*–*K* in *E*. The arrows represent the polarization vectors, and the colors indicate the axial polarization component.

shear modulus of 70 GPa (43). The energy density consumed upon fracture is estimated to be 162 MJ/m^3, while the cyclic energy dissipation density is estimated to be only 0.14 MJ/m^3 per cycle, which is three orders of magnitude smaller, explaining its outstanding fatigue resistance. In comparison, ZrO_2 micropillars have larger hysteresis with energy dissipation density of about 38 MJ/m^3 (12). For BTO micropillars with $\Phi = 1$ μm and 2 μm, the strength is reduced to 4.6 GPa and 2.4 GPa, respectively, and such size effect can be attributed to the "starvation" of preexisting dislocations in the pillars with smaller sizes (37, 44, 45). The SEM images of these micropillars before and after compression tests are illustrated in *SI Appendix*, Fig. S14.

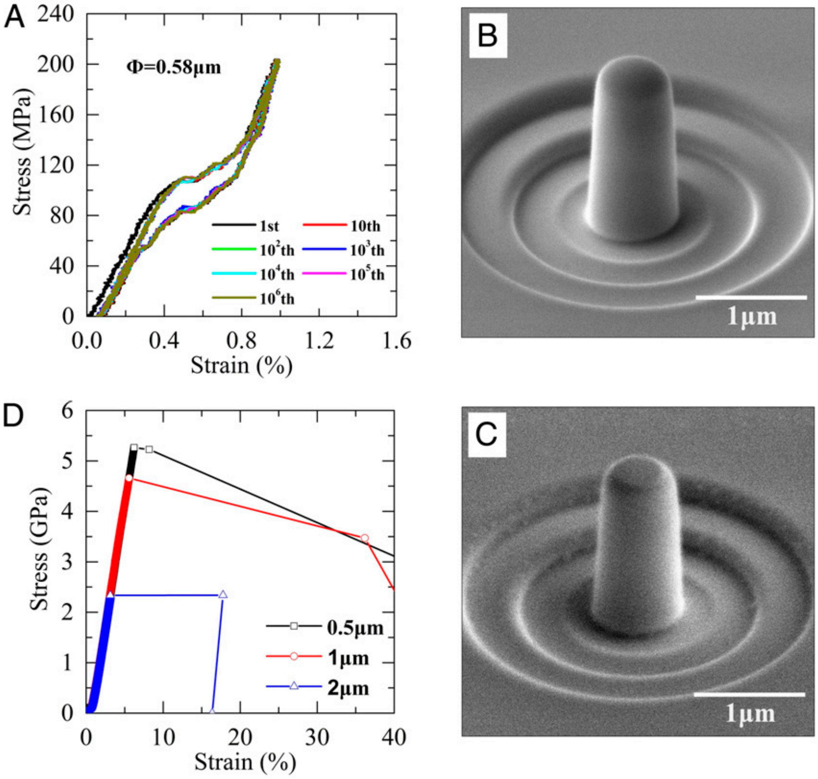

Fig. 3. Fatigue-free BTO micropillars and their ultrahigh strength. (*A*) Cyclic stress–strain curves of BTO micropillar with Φ = 0.58 μm up to one million cycles. SEM images of BTO micropillars with Φ = 0.58 μm before (*B*) and after (*C*) fatigue test. (*D*) Monotonic stress–strain curves for micropillars with Φ = 0.5, 1, and 2 μm.

Comparison with Other Superelastic Materials

Fig. 4 compares the fatigue lives and strengths of our BTO micropillars with other superelastic materials. The fatigue lives of BTO micropillars outperform previous zirconia-based micropillars and particles (12–20) and are on par with NiTi SMA micropillars (10) as well as rubbers (46) (Fig. 4*A*). This is exceptional since bulk BTO is brittle (27, 47), whereas NiTi, CuAlNi, and rubber all enjoy excellent fatigue lives in bulk forms. The stresses needed to

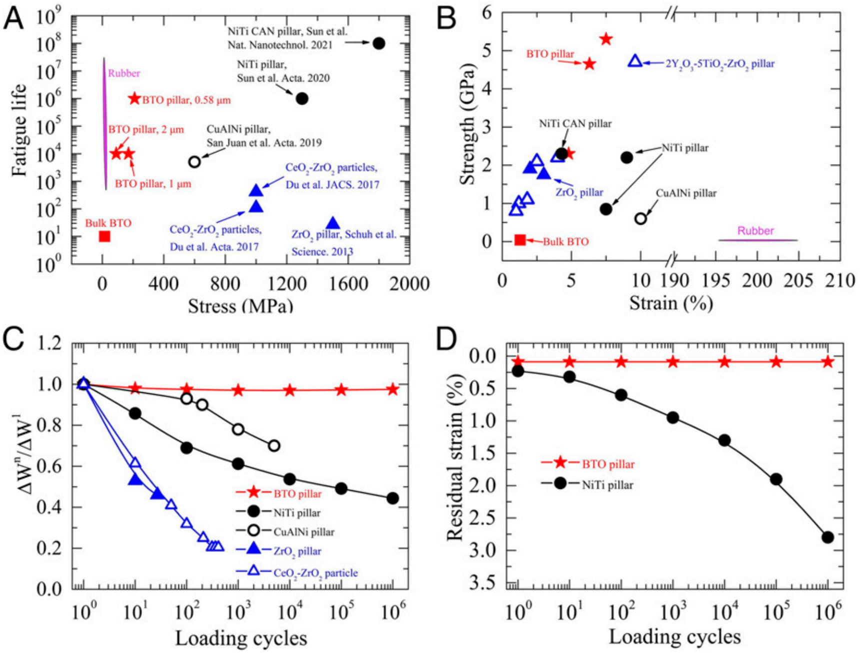

Fig. 4. Comparison of BTO micropillar with other superelastic materials. (*A*) Fatigue life. (*B*) Strength. Variation of normalized energy dissipation (*C*) and residual strain (*D*) over cycling. ΔW^n and ΔW^1 represent the energy dissipated in the *n*th and the first loading cycle, respectively.

realize superelasticity in BTO micropillars are in the range of 40 to 100 MPa, much smaller than SMA and ZrO_2 micropillars, and are only larger than rubber. Furthermore, the ultimate strength of the BTO micropillar is higher than other materials (Fig. 4*B*), partly responsible for its excellent fatigue life as the necessary stress for superelasticity is much smaller. In addition, while other superelastic micropillars suffer from large variations in stress–strain curves during cycling, as measured by the amounts of their normalized energy dissipation (Fig. 4*C*), as well as continuous accumulation of residual strains over cycling (Fig. 4*D*), BTO micropillars are remarkably stable with negligible variation in stress–strain curves and virtually no accumulation of residual strains. Indeed, the energy dissipation of NiTi micropillars varies by about 55% after one million cycles, whereas BTO micropillars only vary by about 3%, with only 0.08% residual strain, most of which was induced in the first cycle. NiTi micropillars, on the other hand, gradually accumulate residual strains of 3% (10). Such drastic differences in cycling stability is due to 90° domain switching in BTO instead of phase transition, which usually has much lower energy barriers (28, 47) and thus much smaller energy dissipation. Furthermore, dislocation generation and motion are very difficult in oxides (26), making plastic deformation negligible.

In summary, we have demonstrated excellent superelasticity with remarkable fatigue resistance of BTO micropillars. The surface tension–modulated 90° domain switching uncovered in superelastic BTO micropillars is advantageous over the conventional phase transition mechanism, and it is distinct from freestanding BTO membranes as well (6, 48). The same mechanism will likely operate in other ferroelectric materials, for example, in $PbTiO_3$ (49), which is expected to generate even larger recoverable strains. While domain switching in ferroelectrics is relatively well understood, and size effect has been widely investigated, our work presents the very first observation that the size-related surface tension can serve as a restoring force for domain switching, resulting in not only superior superelastic behavior but also fatigue-resistant cyclic performance. Such BTO micropillars could potentially be utilized as dampers in micro-electro-mechanical system (MEMS) devices, as pointed out by Lai et al. (6) and San Juan et al. (7–9). This work thus provides understanding to ferroelectrics while demonstrates a promising strategy to realize fatigue-resistant superelasticity in functional oxides.

Materials and Methods

Material Preparation and Characterization. The BTO crystals were provided by the Shanghai Institute of Ceramics, Chinese Academy of Sciences. They are cut along the [001] direction with dimension of 5 × 5 × 1 mm^3 (*SI Appendix*, Fig. S1*A*). The two opposite 5 × 5 mm^2 faces were polished carefully by diamond paste with a roughness of 2 nm. Its Curie temperature is 135 °C, which was determined by measuring the evolution of the dielectric constant as a function of temperature with an impedance analyzer from room temperature (25 °C) to 200 °C (TH2827 Changzhou Tonghui Electronic Co., Ltd), as presented in *SI Appendix*, Fig. S2*A*. The mechanical distortion $S_0 = c/a-1$ measured by XRD method is about 1.05% at 25 °C (*SI Appendix*, Fig. S2*B*).

The electrical poling was conducted at 130 °C with a DC electric field of 500 V/mm. After poling, the domain structure of the specimen was examined by polarized light microscopy to ensure that the sample is fully poled. The polarization of the material is about 26 μC/cm^2 (*SI Appendix*, Fig. S3*A*), characterized by the type Sawyer–Tower circuit. The strain was measured by two strain gauges. Results show that the measured strain is only 0.01%. The mechanical depolarization behavior of bulk BTO single crystal (5 × 5 × 5 mm^3) was also measured. *SI Appendix*, Fig. S3*B* displays the polarization versus stress curve and the strain versus stress curve, from which we can determine that, for the bulk BTO crystal, the critical stress at which domain switching begins is about 2 MPa and that the compressive stress of 15 MPa can completely depolarize the crystal via 90° domain switching, resulting in residual strain as large as 0.95%.

BTO Micropillar Fabrication. Cylindrical micropillars with diameter Φ of 0.5, 1, 2, 3, 4, and 5 μm, respectively, were milled by a dual-beam FIB with the FEI Nano Lab 600i system on the 5 × 5 mm^2 surface of the BTO crystal (*SI Appendix*, Fig. S1), with a successful rate of nearly 100%. The axial direction of the micropillar was selected along the [001] direction to facilitate 90° domain switching under compressive stress, which gives the largest ferroelastic strain. For all micropillars, the ratio of height to diameter is fixed at 3. The taper angle was measured for all micropillars with a value of 2°∼4°.

Prior to fabricating micropillars, a 5 to 10 nm platinum (Pt) film was deposited on the top surface of the BTO sample to enhance conductivity. This thin film was locally removed before milling micropillars by FIB. The fabrication conditions of all micropillars were at 30 kV and 9.3 nA for rough-cut and 26 pA for final polishing using Ion beam of Ga ions. Five pillars were prepared for each size.

Constitutive Behavior of the BTO Micropillars. The stress–strain curves of the BTO micropillars were measured by a nanoindenter (Hysitron TI 950) equipped with a diamond flat-end punch (10 μm) at room temperature (25 °C), with loading directions along the long axis (*SI Appendix*, Fig. S4). The stress σ and the strain ε of micropillars were calculated using $\sigma=|P/A_0|$ and $\varepsilon=|\Delta h/h_0|$, respectively. Here P, Δh, h_0, and A_0 are the applied load, the height reduction, the original height, and the top area of the micropillars, respectively. The monotonic test of micropillar was conducted in triangular waveform with loading-unloading rate of 10 MPa/s, without mechanical holding. The cyclic fatigue test was conducted at 2 Hz under the minimum stress of zero to the set maximum stress. All tests were performed with thermal drift correction in machine system and a high acquisition rate of 1,000 points per second. In particular, a noncontact Bruker NPFLEX 30 surface metrology system was used to measure the height changes of the micropillars after certain cycles of compression, and then the average height difference between the top surface of the micropillars and the bottom substrate is used to calibrate the residual displacement and the residual strain (10).

Measuring the load displacement of the micropillars accurately is challenging due to the inevitable deformation of the substrate, and the effect is corrected by the dual-pillar method developed recently (34). Five micropillars with Φ of 0.5, 1, 2, 3, 4, and 5 μm and heights of only 0.2 μm are fabricated, and their load-displacement curves are measured by nanoindentation. By subtracting the measured displacement of the short pillar from that of the long pillar, accurate stress–strain response of the uniformly deformed middle part of the long pillar can be obtained. The corresponding true strains are calculated as

$$\varepsilon = \left|(\delta_l - \delta_s)/(h_l - h_s)\right|,$$

where ε represents the strain, δ_l is the total deformation of the long micropillars measured by the nanoindentation, δ_s is the deformation of the short micropillars under the same load, and h_l and h_s represent the height of the long and the short pillars. Results demonstrate the overestimation of the axial strain by 10∼20%.

PFM Characterization. The PFM experiments were performed on an asylum research Cypher-ES atomic force microscopy. A FMG01/Pt cantilever with spring constant of 3 N/m and free resonance frequency of 70 kHz was used to characterize the domain structure on the top surface of BTO micropillars with Φ = 2 μm and 5 μm. Vertical and lateral modes were used, and the measured topography, amplitude, and phase maps are illustrated in *SI Appendix*, Fig. S7. With the same cantilever, we also wrote box-in-box domain structure on the top surface of the micropillars using ±40 V DC bias. For micropillar with Φ = 2 μm and 5 μm, the measured results are shown in *SI Appendix*, Fig. S8 *A* and *B*, respectively. The local hysteresis loops of micropillar with Φ = 2 μm and 5 μm were also characterized by switching spectroscopy PFM (SS-PFM) with another ASYELEC.01-R2 cantilever with spring constant of 2.8 N/m and free resonance frequency of 75 kHz (*SI Appendix*, Fig. S8 *C* and *D*).

In Situ TEM Experiment. The specimens with nominal length of 800 nm, nominal width of 620 nm, and nominal thickness of 200 nm for in situ TEM compression were fabricated using FIB. The pillars were milled to ensure that the sides are parallel. In situ pillar compression experiments were performed in the Tecnai F20 (Thermo Fisher Scientific) at an operating voltage of 200 kV. An in situ Hysitron PI95 pico-indenter with a flat tip was used, and micropillar alignment was monitored with bright-field imaging to ensure that the surface of the micropillar was parallel with the indenter surface. The experiment was performed in displacement control mode with a displacement rate of 1 nm/s. *SI Appendix*, Fig. S9 displays the loading waveform and the microstructure in BTO micropillar during loading and unloading, corresponding to the points of **b** to **e** in *SI Appendix*, Fig. S9*A*. *SI Appendix*, Fig. S9*F* reveals the TEM images of the sample after damage. The detailed domain structure evolution process can be seen more clearly in Movie S1. We sped up the video to make it easier to watch.

Here, it should be noted that, different from the pillar with circular cross section, the cross section of the pillar we used for in situ TEM observation is a rectangle, with dimension of 200 nm × 620 nm. The curvature radius Φ of the surfaces for this rectangle pillar is infinity. As a result, the lateral compressive stress, which can be estimated by $\sigma_{11} = \sigma_{22} = 2\gamma/\Phi$, is zero ($\gamma$ is the surface tension or surface energy). Therefore, some a-c domain walls can exist stably in this pillar.

Phase Field Modeling. The free energy density for the ferroelectric phase BTO material can be written as

$$F = \alpha_{ij}P_iP_j + \alpha_{ijkl}P_iP_jP_kP_l + \alpha_{ijklmn}P_iP_jP_kP_lP_mP_n + \alpha_{ijklmnpq}P_iP_jP_kP_lP_mP_nP_pP_q + \frac{1}{2}c_{ijkl}\varepsilon_{ij}\varepsilon_{kl} - q_{ijkl}\varepsilon_{ij}P_kP_l + \frac{1}{2}g_{ijkl}P_{i,j}P_{k,l} - \kappa_0\kappa_rE_iE_i - E_iP_i, \quad [1]$$

in which the repeating subscripts imply summation over the Cartesian coordinate components x_i ($i = 1, 2, 3$) with "i" denoting the partial derivative operator with respect to x_i. α_{ij}, α_{ijkl}, α_{ijklmn}, and $\alpha_{ijklmnpq}$ representing Landau expansion coefficients; c_{ijkl}, q_{ijkl}, and g_{ijkl} correspond to the elastic, electrostrictive, and gradient coefficients, respectively. ε_0 is the vacuum permittivity, and ε_r denotes the relative dielectric constant of the background material (cubic BTO in this case), P_i, ε_{ij}, and E_i are the polarization, strain, and electric field components, respectively.

For an ideal ferroelectric material without body charge and body force, the spatial and temporal evolution of the field variables are governed by the time-dependent Ginzburg–Landau equation coupled with the mechanical equilibrium equations and Maxwell's equations as

$$\frac{\partial P_i}{\partial t} = -L\left(\frac{\partial F}{\partial P_i} - \frac{\partial}{\partial x_j}\frac{\partial F}{\partial P_{i,j}}\right), \quad [2]$$

$$\sigma_{ij,i} = \frac{\partial}{\partial x_i}\frac{\partial F}{\partial \varepsilon_{ij}} = 0\,, \quad [3]$$

$$D_{i,i} = -\frac{\partial}{\partial x_i}\frac{\partial F}{\partial E_i} = 0\,, \quad [4]$$

where t is the time and L denotes the kinetic coefficient. σ_{ij} and D_i represent the mechanical stress and electric displacement, respectively.

A nonlinear finite element method is used to solve the governing Eqs. **2**–**4**, and all of the coefficients are identical to those listed in ref. 50. In the simulation, the bottom of micropillars are mechanically fixed, and open circuit boundary condition is applied on all surfaces. In the phase field simulation, the surface tension–induced stress $\sigma_{11} = \sigma_{22} = 2\gamma/\Phi$ is applied as the radial compressive stress on the side surface, which is inversely proportional to the radius of surface curvature of the micropillar (31, 32). Here, γ means the surface energy (or surface tension), with typical values vary between 5 N/m and 50 N/m (31, 32, 51, 52). In this article, we set it to 30 N/m. Φ represents the diameter of the BTO micropillar. At the beginning of the simulation, a Gaussian random distribution of polarization was introduced to initiate the polarization evolution process.

Data Availability. All data are available in the article and/or *SI Appendix*.

ACKNOWLEDGMENTS. We acknowledge the support from the National Key Research and Development Program of China (Grant 2016YFA0201001), National Natural Science Foundation of China (Grants 11972262, 11627801, 11672264, 11972320, 52021006, and 11974023), the support of Guangdong Provincial Key Laboratory Program from the Department of Science and Technology of Guangdong Province (Grant 2021B1212040001), the Natural Science Foundation of Hubei Province (Grant 2019CFB486), the Fundamental Research Funds for the Central Universities, the Fundamental Research Program of Shenzhen (Grant JCYJ20170412153039309), and Zhejiang Provincial Natural Science Foundation (Grant LZ17A020001). This work was also supported by the Pico Center at SUSTech that receives support from Presidential fund and Development and Reform Commission of Shenzhen Municipality, the Science, Technology, and Innovation Commission of Shenzhen Municipality (Grant SGDX2019081623360564), the open foundation of Hubei Key Laboratory of Theory and Application of Advanced Materials Mechanics (Wuhan University of Technology) (Grant TAM202002).

1. K. Otsuka, X. B. Ren, Physical metallurgy of Ti–Ni-based shape memory alloys. *Prog. Mater. Sci.* **50**, 511–678 (2005).
2. L. R. G. Treloar, *The Physics of Rubber Elasticity* (Oxford University Press, Oxford, ed. 3, 2005).
3. J. M. Jani, M. Leary, A. Subic, M. A. Gibson, A review of shape memory alloy research applications and opportunities. *Mater. Des.* **56**, 1078–1113 (2014).
4. K. Bhattacharya, R. D. James, Applied physics. The material is the machine. *Science* **307**, 53–54 (2005).
5. D. C. Lagoudas, *Shape Memory Alloys: Modeling and Engineering Applications* (Springer, New York, ed. 1, 2010).
6. G. Dong *et al.*, Super-elastic ferroelectric single-crystal membrane with continuous electric dipole rotation. *Science* **366**, 475–479 (2019).
7. J. San Juan, M. L. Nó, C. A. Schuh, Nanoscale shape-memory alloys for ultrahigh mechanical damping. *Nat. Nanotechnol.* **4**, 415–419 (2009).
8. J. F. Gómez-Cortés *et al.*, Size effect and scaling power-law for superelasticity in shape-memory alloys at the nanoscale. *Nat. Nanotechnol.* **12**, 790–796 (2017).
9. J. F. Gómez-Cortés *et al.*, Ultrahigh superelastic damping at the nano-scale: A robust phenomenon to improve smart MEMS devices. *Acta Mater.* **166**, 346–356 (2019).
10. P. Hua, K. J. Chu, F. Z. Ren, Q. P. Sun, Cyclic phase transformation behavior of nanocrystalline NiTi at microscale. *Acta Mater.* **185**, 507–517 (2020).
11. K. Bhattacharya, S. Conti, G. Zanzotto, J. Zimmer, Crystal symmetry and the reversibility of martensitic transformations. *Nature* **428**, 55–59 (2004).
12. A. Lai, Z. Du, C. L. Gan, C. A. Schuh, Shape memory and superelastic ceramics at small scales. *Science* **341**, 1505–1508 (2013).
13. Z. H. Du *et al.*, Superelasticity in micro-scale shape memory ceramic particles. *Acta Mater.* **123**, 255–263 (2017).
14. Z. H. Du *et al.*, Size effects and shape memory properties in ZrO_2 ceramic micro- and nano-pillars. *Scr. Mater.* **101**, 40–43 (2015).
15. X. M. Zeng *et al.*, Microstructure, crystallization and shape memory behavior of titania and yttria co-doped zirconia. *J. Eur. Ceram. Soc.* **36**, 1277–1283 (2016).
16. Z. H. Du *et al.*, Synthesis of monodisperse CeO_2-ZrO_2 particles exhibiting cyclic superelasticity over hundreds of cycles. *J. Am. Ceram. Soc.* **100**, 4199–4208 (2017).
17. X. M. Zeng *et al.*, Crystal orientation dependence of the stress-induced martensitic transformation in zirconia-based shape memory ceramics. *Acta Mater.* **116**, 124–135 (2016).
18. X. M. Zeng *et al.*, Enhanced shape memory and superelasticity in small-volume ceramics: A perspective on the controlling factors. *MRS Commun.* **7**, 747–754 (2017).
19. E. L. Pang, C. A. McCandler, C. A. Schuh, Reduced cracking in polycrystalline ZrO_2-CeO_2 shape- memory ceramics by meeting the cofactor conditions. *Acta Mater.* **177**, 203–239 (2019).
20. J. Jetter *et al.*, Tuning crystallographic compatibility to enhance shape memory in ceramics. *Phys. Rev. Mater.* **3**, 093603 (2019).
21. C. Lee, X. Wei, J. W. Kysar, J. Hone, Measurement of the elastic properties and intrinsic strength of monolayer graphene. *Science* **321**, 385–388 (2008).
22. A. Banerjee *et al.*, Ultralarge elastic deformation of nanoscale diamond. *Science* **360**, 300–302 (2018).
23. A. G. Evans, Fatigue in ceramics. *Int. J. Fract.* **16**, 485–498 (1980).
24. S. Horibe, R. Hirahara, Cyclic fatigue of ceramic materials: Influence of crack path and fatigue mechanisms. *Acta Metall. Mater.* **39**, 1309–1317 (1991).
25. C. Chluba *et al.*, Shape memory alloys. Ultralow-fatigue shape memory alloy films. *Science* **348**, 1004–1007 (2015).
26. P. R. Ren *et al.*, High temperature creep-mediated functionality in polycrystalline barium titanate. *J. Am. Ceram. Soc.* **103**, 1891–1902 (2020).
27. D. N. Fang, Y. J. Jiang, S. Li, C. T. Sun, Interactions between domain switching and crack propagation in poled $BaTiO_3$ single crystal under mechanical loading. *Acta Mater.* **55**, 5758–5767 (2007).
28. E. Burcsu, G. Ravichandran, K. Bhattacharya, Large electrostrictive actuation of barium titanate single crystals. *J. Mech. Phys. Solids* **5**, 2823–2846 (2004).
29. Y. W. Li, F. X. Li, Ultrahigh actuation strains in $BaTiO_3$ and $Pb(Mn_{1/3}Nb_{2/3})O_3$-$PbTiO_3$ single crystals via reversible electromechanical domain switching. *Appl. Phys. Lett.* **102**, 152905 (2013).
30. X. B. Ren, Large electric-field-induced strain in ferroelectric crystals by reversible domain switching. *Nat. Mater.* **3**, 91–94 (2004).
31. A. N. Morozovska, E. A. Eliseev, M. D. Glinchuk, Ferroelectricity enhancement in confined nanorods: Direct variational method. *Phys. Rev. B Condens. Matter Mater. Phys.* **73**, 214106 (2006).
32. M. J. Zhou *et al.*, Nanopore-induced dielectric and piezoelectric enhancement in PbTiO3 nanowires. *Acta Mater.* **187**, 146–152 (2020).
33. K. J. Choi *et al.*, Enhancement of ferroelectricity in strained BaTiO3 thin films. *Science* **306**, 1005–1009 (2004).
34. K. J. Chu, K. Yan, F. Z. Ren, Q. P. Sun, A dual-pillar method for measurement of stress-strain response of material at microscale. *Scr. Mater.* **172**, 138–143 (2019).
35. P. M. Rørvik, T. Grande, M. A. Einarsrud, One-dimensional nanostructures of ferroelectric perovskites. *Adv. Mater.* **23**, 4007–4034 (2011).
36. J. Diao, K. Gall, M. L. Dunn, Surface-stress-induced phase transformation in metal nanowires. *Nat. Mater.* **2**, 656–660 (2003).
37. M. D. Uchic, D. M. Dimiduk, J. N. Florando, W. D. Nix, Sample dimensions influence strength and crystal plasticity. *Science* **305**, 986–989 (2004).

38. Q. Yu *et al*., Strong crystal size effect on deformation twinning. *Nature* **463**, 335–338 (2010).
39. E. Camposilvan, M. Anglada, Size and plasticity effects inzirconia micropillars compression. *Acta Mater.* **103**, 882–892 (2016).
40. P. Hua, M. Xia, Y. Onuki, Q. Sun, Nanocomposite NiTi shape memory alloy with high strength and fatigue resistance. *Nat. Nanotechnol.* **16**, 409–413 (2021).
41. M. J. Polking *et al*., Ferroelectric order in individual nanometre-scale crystals. *Nat. Mater.* **11**, 700–709 (2012).
42. Y. W. Li *et al*., Large and electric field tunable superelasticity in BaTiO3 crystals predicted by an incremental domain switching criterion. *Appl. Phys. Lett.* **102**, 092905 (2013).
43. G. J. Fischer, Z. C. Wang, S. I. Karato, Elasticity of $CaTiO_3$, $SrTiO_3$ and $BaTiO_3$ perovskites up to 3.0 Gpa: The effect of crystallographic structure. *Phys. Chem. Miner.* **20**, 97–103 (1993).
44. J. R. Greer, W. C. Oliver, W. D. Nix, Size dependence of mechanical properties of gold at the micron scale in the absence of strain gradients. *Acta Mater.* **53**, 1821–1830 (2005).
45. J. A. El-Awady, Unravelling the physics of size-dependent dislocation-mediated plasticity. *Nat. Commun.* **6**, 5926 (2015).
46. C. S. Woo, W. D. Kim, J. D. Kwon, A study on the material properties and fatigue life prediction of natural rubber component. *Mater. Sci. Eng. A.* **483**, 376–381 (2008).
47. Y. W. Li, F. X. Li, Domain switching criterion for ferroelectric single crystals under uniaxial electromechanical loading. *Mech. Mater.* **93**, 246–256 (2016).
48. B. Peng *et al*., Phase transition enhanced superior elasticity in freestanding single-crystalline multiferroic $BiFeO_3$ membranes. *Sci. Adv.* **6**, 1–9 (2020).
49. L. Zhang *et al*., Giant polarization in super-tetragonal thin films through interphase strain. *Science* **361**, 494–497 (2018).
50. L. Q. Chen, *Physics of Ferroelectrics* (Springer, Berlin), vol. 105, pp. 363–372 (2007).
51. W. H. Ma, M. S. Zhang, Z. H. Lu, A study of size effects in PbTiO3 nanocrystals by Raman spectroscopy. *Phys. Status Solidi A Appl. Res.* **166**, 811–815 (1998).
52. Y. Zheng, C. H. Woo, B. Wang, Surface tension and size effect in ferroelectric nanotubes. *J. Phys. Condens. Matter* **20**, 135216–135224 (2008).